THE IONIZATION CONE, OBSCURED NUCLEUS, AND GASEOUS OUTFLOW IN NGC 3281: A PROTOTYPICAL SEYFERT 2 GALAXY?

THAISA STORCHI-BERGMANN
Instituto de Fisica, UFRGS, Campus do Vale, C.P. 15051, 91500-P. Alegre, RS, Brasil; and Astronomy Department, University of Maryland

ANDREW S. WILSON[1]
Astronomy Department, University of Maryland; and Space Telescope Science Institute, 3700 San Martin Drive, Baltimore, MD 21218

AND

JACK A. BALDWIN
Cerro Tololo Inter-American Observatory, National Optical Astronomy Observatories,[2] Casilla 603, La Serena, Chile

ABSTRACT

We present narrow-band images and long-slit spectroscopy of the central region of the highly inclined Seyfert galaxy NGC 3281. The image of the continuum-subtracted [O III] $\lambda 4959$ emission line shows a very clear conical morphology for the high-excitation gas, which seems to extend to a large distance (≈ 2 kpc) above the disk of the galaxy. A possible similar structure can also be seen on the other side of the nucleus, but is dimmed by patchy obscuration in the disk. Using the continuum images and long-slit spectroscopy, we derive and map the extinction in the inner regions of NGC 3281, and find heavy obscuration along our line of sight to the apex of the cone. This result suggests that the true nucleus is located at the apex and is obscured.

Low-resolution long-slit spectra are used to study the stellar population, which is found to be old, uniform within 2.5 kpc of the nucleus and typical of the bulges of early-type galaxies. No dilution was observed in the absorption lines in any of the extracted spectra, confirming that the nuclear nonstellar source is obscured. The equivalent width of the Na I D absorption line is strongly correlated with the reddening of the starlight and, after subtraction of the contribution from stellar atmospheres, is used to map the interstellar obscuration. After subtraction of a "template" representing the stellar population, the fluxes of the emission lines are obtained, and maps showing the spatial distribution of emission-line ratios are constructed. These ratios are then compared with model calculations in order to investigate the nature of the ionizing source and characteristics of the emitting gas. According to these models, the abundances of nitrogen and sulfur in the gas are 3 times the solar value and the ionization parameter increases away from the apex along the axis of the cone. The density profile along the axis of the cone is obtained from the [S II] $\lambda\lambda 6717, 6731$ doublet and compared with that predicted for a wind and for an hydrostatic atmosphere.

Higher resolution long-slit spectra are used to study the kinematics of the emitting gas. A circular velocity model, intended to represent a rotational component of motion, is computed and subtracted from the observed gas velocities. The residuals indicate the presence of an outflow from the nucleus at 150 km s^{-1} within the cone. Observed double-peaked profiles are consistent with this interpretation.

A comparison between the upper limit to the number of ionizing photons ($N_{\rm ion}$) inferred from the optical continuum and the observed number of Balmer recombination photons ($N_{\rm rec}$) reveals a large discrepancy [$N_{\rm rec}/(N_{\rm ion} C) > 490$, where C is the covering factor of optically thick gas as seen from the nucleus]. The nuclear ionizing source is, therefore, blocked from direct view ($A_V \geq 6$ mag if the source radiates isotropically), apparently through shadowing by the dusty torus that hides the nucleus. The luminosity of the ionizing source is obtained from the emission line properties and used to predict the mid- and far-infrared luminosity produced through reprocessing by dust in the torus. This luminosity ($5.3 \pm 2.2 \times 10^{10}\ L_{\odot}$) is consistent with that inferred from the IRAS fluxes.

All of the above characteristics are expected in "unified" models of AGNs, in which Seyfert 2's contain a Seyfert 1 nucleus which is hidden from direct view by an obscuring torus. We therefore suggest that NGC 3281 may be another example of a "hidden" Seyfert 1, even though there is no direct evidence for a broad-line region in this particular galaxy.

Subject headings: galaxies: individual (NGC 3281) — galaxies: kinematics and dynamics — galaxies: nuclei — galaxies: Seyfert

1. INTRODUCTION

The discovery by Antonucci & Miller (1985) of broad polarized Balmer lines in the spectrum of the Seyfert 2 galaxy NGC 1068 has led to the currently popular "Unified Scheme" for radio-quiet active galactic nuclei: in this scenario, Seyfert 2 galaxies are Seyfert 1's in which the nuclear source and the broad-line region are hidden from direct view, probably behind an obscuring torus. This torus shadows the escaping ionizing radiation, leading to conical morphologies in the high-excitation gas. In the model of Krolik & Begelman (1986), a wind driven by the nuclear continuum is also predicted.

Several observations support this scenario: apparent "photon deficits," in which extrapolation of the observed ultraviolet continua provides too few ionizing photons to account for the observed Balmer emission, suggesting our view of the continuum nucleus is blocked (Wilson, Ward, & Haniff 1988; Kinney et al. 1991); the discovery of more Seyfert 2 galaxies with broad Balmer lines visible in polarized light (Miller & Goodrich 1990); narrow-line regions aligned with the radio axes (Haniff, Wilson, & Ward 1988); and conical structures in the high-excitation gas in several Seyfert 2 galaxies, e.g., NGC 1068 (Pogge 1988), NGC 4388 (Corbin, Baldwin, & Wilson 1988), NGC 5252 (Tadhunter & Tsvetanov 1989), NGC 1365 and NGC 7582 (Storchi-Bergmann & Bonatto 1991 and references therein for other examples). In the case of the last two galaxies, gaseous outflows within the ionization cone have also been observed (Phillips et al. 1983c; Morris et al. 1985), a phenomenon also found in Mrk 509 (Phillips et al. 1983a) and possibly in NGC 5506 (Wilson, Baldwin, & Ulvestad 1985).

In the present paper, we analyze narrow band images and long-slit spectroscopy of NGC 3281, another nearby Seyfert 2 galaxy which we find to be a new example of the success of the "Unified Scheme." While in many Seyfert 2's evidence for this model is limited or ambiguous, NGC 3281 shows most of the expected features: an ionization cone, heavy obscuration at the apex of the cone (presumably hiding the true nucleus), a wind outflow along the cone, and emission-line ratios which are consistent with photoionization by a power-law continuum.

NGC 3281 was described by Sandage (1978) as belonging to the Antlia group, with a "high-excitation' spectrum ([O III] $\lambda5007 \gg H\beta$) and a strong Na I D line in absorption. Phllips, Charles, & Baldwin (1983a) classified this galaxy as a Seyfert 2 on the basis of the emission-line ratios, but pointed out that the luminosity of the lines is lower than in typical Seyfert's 2. In this respect, it is similar to NGC 1386 (Weaver, Wilson & Baldwin 1991). Sandage (1978) classified NGC 3281 as SA(s)a, while de Vaucouleurs, de Vaucouleurs, & Corwin (1976, hereafter RC2) preferred SA(s)b?. Durret & Bergeron (1988), using long-slit spectroscopy, have reported the presence of an "extended ionized envelope" with diameter $\approx 20''$.

Observations with the Parkes 64 m telescope (Reif et al. 1982) have given only an upper limit to the flux of the H I 21 cm line (integrated flux density <11.4 Jy km s^{-1}). Ulvestad & Wilson (1989) observed NGC 3281 with the VLA, finding radio continuum fluxes of 61.2 mJy (20 cm) and 26.7 mJy (6 cm) from an unresolved nuclear source. An upper limit to the flux of the CO $J = 1$–0 line of 2.4 K km s^{-1} was obtained by Heckman et al. (1989) with the NRAO 12 m telescope.

NGC 3281 is also an *IRAS* source with $L_{IR} = 3.4 \times 10^{10} L_\odot$ and infrared spectral indexes $\alpha(60, 25) = -1.11$ and $\alpha(100, 60) = -0.25$ (with $S \propto \nu^\alpha$; data from the *IRAS* Point Source Catalog 1985). These spectral indices fall in the range occupied by Seyfert 2 galaxies. Near-infrared photometric data are given in Boisson & Durret (1986).

Rubin et al. (1985, hereafter RBFT) have obtained the rotation curve of NGC 3281. They used emission lines more than 10'' from the nucleus because non circular motions are observed closer in. Since our own observations refer mainly to the nuclear vicinity, we decided to adopt the systemic velocity obtained by these authors: 3396 ± 20 km s^{-1} (heliocentric) or 3115 km s^{-1} (after correction for the solar motion with respect to the Local Group). With $H_0 = 75$ km s^{-1} Mpc^{-1} the distance of the galaxy is then 41.5 Mpc, and the angular scale is 1'' = 201 pc, which will be used throughout the paper.

2. OBSERVATIONS

2.1. *Direct Imaging*

Direct images of NGC 3281 were obtained at the Cerro Tololo Inter-American Observatory (CTIO) 1.5 m and 4 m telescopes using CCD detectors. A log of the observations is given in Table 1.

The individual images were corrected for bias and flat-fielded. As they were obtained with two different telescopes, with different spatial scales, the images were interpolated onto a common grid using field stars as references. The point-spread functions (PSFs) of the line plus continuum and the continuum images were compared, and the one with the smaller PSF was convolved with a Gaussian function in order to match the one with the larger PSF. Each continuum image was then scaled by a factor such that the integrated number of counts for the stars in the field was equal to the corresponding value in the adjacent line plus continuum frame. Finally, images in [O III] $\lambda4959$ and Hα + [N II] $\lambda\lambda6548$, 6583 were produced by subtracting the appropriate continuum frame from the line plus continuum frame.

2.2. *Long-Slit Spectroscopy*

Two series of long-slit spectroscopic observations of NGC 3281 have been made with a 40 mm SIT Vidicon detector on the Ritchey-Chrétien (RC) spectrograph attached to the CTIO 4 m telescope. A third set of observations was obtained with a CCD detector on the same spectrograph and telescope. A log of the observations in shown in Table 2.

The first set of observations, covering the spectral range 4200–5350 Å, with resolution 1.8 Å, was taken to investigate the kinematics of the extended nebulosity, as revealed by the velocities of Hβ and [O III] $\lambda\lambda4959$, 5007. The slit was oriented at a position angle (p.a.) 137°, which lies approximately along the photometric major axis of the galaxy. Spectra were obtained at 13 slit positions, with the first passing through the nucleus and the others at 1''.5, 3''.0, 4''.5, 6''.0, 7''.5 and 9''.0 to the NE and SW of the nucleus, the slit being moved perpendicular to its length. As the slit width was 1''.5, the circumnuclear gas was fully sampled by this grid. The exposures with the slit displaced 9''.0 NE and SW and 7''.5 NE from the nucleus showed no line emission. A grid of adjacent spectra was

TABLE 1

CCD IMAGES OF NGC 3281

Telescope	Filter (Å/ΔÅ)	Exposure (minutes)	Scale (arcsec pixel^{-1})	Date (1984 Mar)	Comments
4 m	5007/50	15	0.56	29/30	[O III] $\lambda4959$
	5461/80	15	0.56	29/30	Continuum
1.5 m	6600/110	45	0.40	27/28	Hα + [N II] $\lambda\lambda6548$, 6583
	7080/100	45	0.40	27/28	Continuum

TABLE 2

LONG-SLIT SPECTRA

Parameter	SIT (1)	SIT (2)	CCD
Detector	40 mm SIT Vidicon	40 mm SIT Vidicon	GEC CCD
Dates	1983 Jan 4, 5	1983 Feb 4, 5, 6	1990 Mar 1/2
Spectral region (Å)	4200–5350	3600–7000	3600–7000
Resolution (Å)	1.8	5	11
Slit width	1".5	1".5	1".5
Scale (arcsec pixel^{-1})	0.8	1.2	0.73
Exposure (minutes)	3 (through nucleus) 15–20 (other locations)	4 (through nucleus) 20 (other locations)	20
Extractions	1".6 (2 pixels)	2".4 (2 pixels)	1".46 (2 pixels)
Resolution at galaxy (pc)	300 × 320	300 × 480	300 × 290

extracted from each two-dimensional image, in which two spatial pixels were binned together, giving a spatial resolution along the slit of 1".6.

The second set of observations covered the range 3600–7000 Å at 5 Å resolution in order to obtain information on the ionization structure, excitation conditions, gas density, and reddening. The slit positions were the same as in the first set of observations, and in the extractions two pixels were again binned together, giving a spatial resolution of 2".4.

The last set of observations covered the same spectral range as the second. Data were taken at three slit positions: first, at p.a. = 137° (major axis) through the nucleus; second, at p.a. = 10° through the nucleus; and third, at the same p.a. as the second, but with the slit offset 2" from the nucleus in p.a. = −80°. Except for a few cases, two pixels were binned together, leading to 1".46 spatial resolution along the slit. The exceptions corresponded to distances from the nucleus in excess of 10", for which slit lengths of about 5" were extracted in order to improve the signal-to-noise ratio. This set of CCD spectra has a much better signal to noise ratio than the previous SIT ones.

3. RESULTS

3.1. *Morphology*

The green continuum ($\lambda 5461$) image is displayed in Figure 1. It can be seen that an outer arm extends from the SE corner of the image to outside the field of view. The apparent change in the major axis p.a. at the different isophotal levels is an effect of the spiral structure. We have adopted p.a. = 137° for the major axis, which can be compared with the value p.a. = 138° from RBFT. The dimensions of the major and minor axes at the 2 σ isophotes are then $2a = 184"$ (37.1 kpc) and $2b = 82"$ (16.4 kpc). The RC2 value for the diameter of the major axis at the 25th magnitude isophotal level is 199", indicating that our 2 σ isophotes did not quite reach this magnitude. Using these measurements, we find an inclination $i = 64°$, on the assumption of a thin disk; from the RC2 data one obtains $i = 58°$, while RBFT give $i = 69°$. The inclination is, in any case, uncertain because of the outer spiral structure and we decided to adopt our value of $i = 64°$.

From the direction of winding of the spiral arms (assuming that they are trailing) and from the observed velocity field (§ 3.5), the orientation of the galaxy can be derived: the SW is the near and the NE is the far side of the disk. The presence of a dust lane to the SW of the nucleus confirms this orientation.

Figure 2 shows the continuum-subtracted [O III] image superposed on the green continuum image. A very clear structure is seen protruding toward the NE from the nucleus. This structure resembles the projection of a cone extending to high latitudes relative to the plane of the galaxy. The size of the cone at the 2 σ level from its apex to the NE edge is 8".6 (1.7 kpc). The peak of the [O III] emission is displaced 1".5 (300 pc) NNE of the nucleus (considered as the peak in the green continuum image). Further, the apex of the cone does not coincide with the peak of the continuum light, but is displaced $\approx$ 1".5 (300 pc) SW of it. An absorption lane passes just south of the nucleus, while still farther south (5"–8" [1–1.6 kpc] from the continuum peak), an elongated emission feature is apparent. This feature may be emission from a counterpart to the conical structure seen to the NE. While the NE cone is clearly visible because it projects against the *far* side of the disk, any cone to the SW is obscured by dust in the intervening disk of the galaxy. Also seen to the NE is a detached knot of emission at a projected distance of 12".3 (2.5 kpc) from the nucleus.

The continuum-subtracted Hα + [N II] image is shown in Figure 3a. It presents a similar structure to that seen in the [O III] image. The main differences are that the Hα + [N II] light is less affected by the absorption lane mentioned above, and that the peak of the line emission is almost coincident with the peak of the continuum.
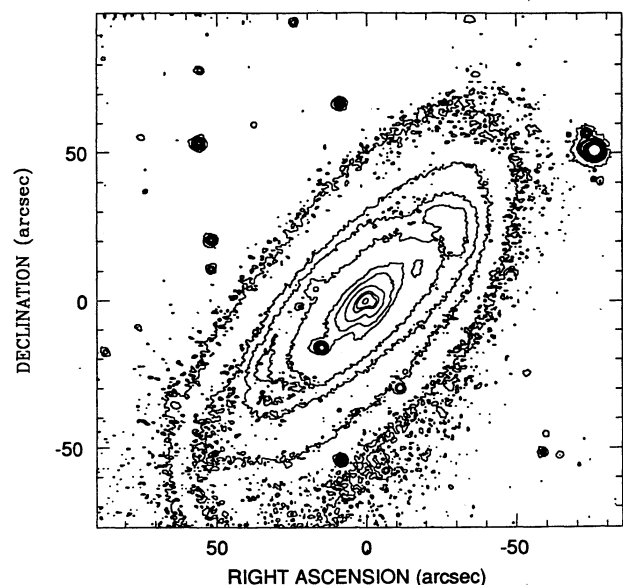

FIG. 1.—Continuum ($\lambda 5461$) isophotes of NGC 3281. Contours are 1%, 3%, 5%, 7.5%, 15%, 20%, 30%, 50%, 75%, and 90% of the peak brightness above the sky. North is to the top, and east to the left.
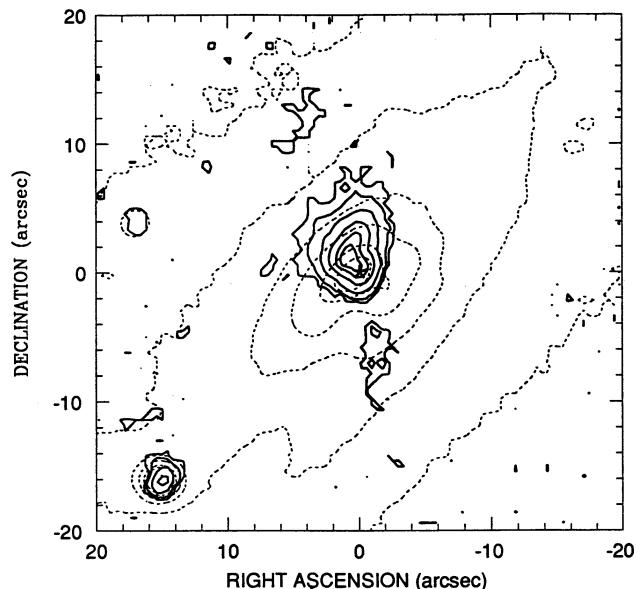
FIG. 2.—Contours of the continuum-subtracted [O III] $\lambda4959$ emission (*continuous lines*) at 5%, 10%, 25%, 50%, 75%, and 90% of the peak brightness above the sky, superposed on contours of the $\lambda5461$ continuum (*dashed lines*); the starred symbol represents the peak of the $\lambda5461$ continuum.

We have constructed an excitation map by dividing the [O III] image by the Hα + [N II] image. This map is shown in Figure 3*b*. Because the images were not flux-calibrated, only relative line ratios can be determined. It can be seen from the figure that the ratios are larger toward the open end of the cone, indicating either decreasing reddening or increasing gaseous excitation (or both) from south to north. In the detached knot to the NE, only [O III] emission is detected, which implies a high excitation there.

Finally, we have divided the red continuum by the green continuum image. This ratio is sensitive to both the stellar population and the interstellar reddening. We have concluded (see § 3.2) that the continuum spectrum of the stellar population of this galaxy is essentially flat (in F_λ) for wavelengths

larger than about 5400 Å: the ratio between the flux in our red continuum filter and that in our green continuum filter for the template which best represents the stellar population is 1.00 ± 0.05. Observed values of this ratio which are greater than 1 are then indicative of reddening. We have set the ratio of the two continuum images equal to unity at locations where the stellar population shows no reddening (as determined from the spectroscopic observations). In this way, we were able to quantify the reddening in terms of $E(B-V)$, considering that a flux ratio equal to 1 corresponds to $E(B-V) = 0$. The resulting values of $E(B-V)$ range from 0.1 to 0.45, in agreement with the values obtained from the stellar population analysis (§ 3.2). This "reddening map" is shown in Figure 4. From the figure, it can be seen that the locus of highest obscuration coincides with the apex of the conical structure seen in [O III]. This strongly suggests that *the true nucleus of the galaxy is hidden behind the absorption lane and does not correspond to the peak in the green continuum.*

3.2. *Stellar Population*

We have used the CCD spectra to study the stellar population in the nuclear region of NGC 3281. The signal-to-noise ratio was adequate for this analysis within a region with dimensions of about 22″ along the major axis and 10″ along the minor axis. This translates, after deprojection into the disk plane, to a region of radius about 2.3 kpc around the nucleus. Inside this region, no gradient was observed in the equivalent width (W) of any observation line except Na I D, indicating that the stellar population is very uniform. We have listed in Table 3 the average W value for each line. The standard deviation of the individual W values is about 1 Å. No dilution of the absorption lines by a featureless continuum was found in the spectra near the nucleus; this gives support to the evidence from the images that the true nucleus is hidden.

The only significant gradient in the equivalent width of an absorption line was found for W(Na I) (window 5880–5914 Å) as the slit crosses the band of obscuration to the south of the nucleus. The values of W(Na I) range from 3 to 6.5 Å. As no similar variation is seen in the other W values, it is clear that W(Na I) contains a contribution from interstellar absorption in
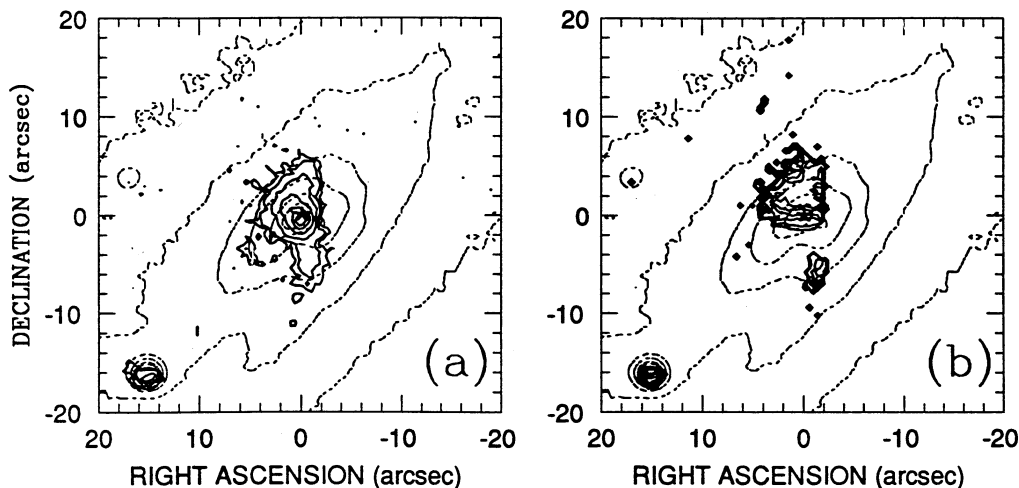

FIG. 3.—(*a*) Contours of the continuum-subtracted Hα + [N II] $\lambda\lambda6548$, 6584 emission (*continuous lines*) at 5%, 10%, 25%, 50%, 75%, and 90% of the peak brightness above the sky superposed on contours of the $\lambda5461$ continuum (*dashed lines*); the starred symbol represents the peak of the $\lambda5461$ continuum (*b*) The solid lines represent the "excitation map", the result of dividing the [O III] $\lambda4959$ map by the Hα + [N II] $\lambda\lambda6548$, 6584 map. The highest contour corresponds to 10 times the value of the lowest one, and the dashed lines are as in (*a*).
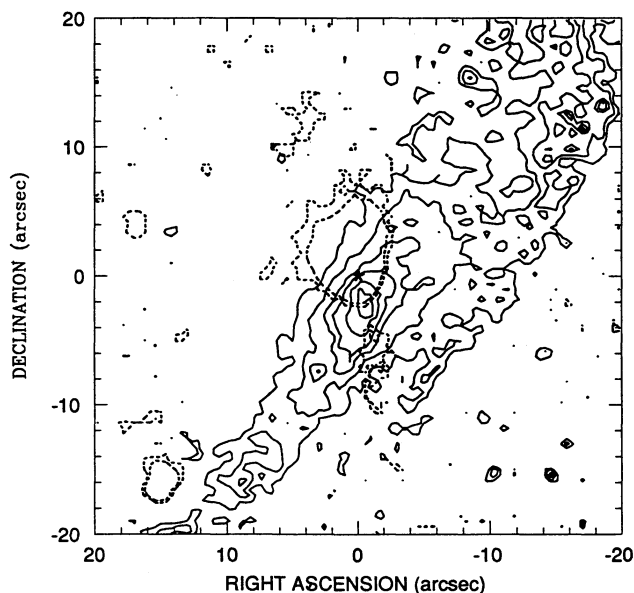
Fig. 4.—Ratio between the two continuum images $\lambda7080/\lambda5461$ (*continuous lines*). Using information about the stellar population (see § 3.1), this ratio translates to a "reddening map" with contour levels corresponding to $E(B-V) = 0.1, 0.2, 0.3, 0.35, 0.40, 0.45$. Also shown, for reference, are the two outermost isophotes of the continuum subtracted [O III] image (*dashed lines*). The starred symbol represents the peak of the $\lambda5461$ continuum.

NGC 3281 (e.g., Bica & Alloin, 1986). Figure 5*a* shows the variation of W(Na I) with position in the galaxy. It can be seen that the high values concentrate in the region of the absorption band discussed above, nicely mapping the interstellar obscuration.

On the basis of the observed W's, we have selected a template to represent the stellar population using the library of synthetic spectra given by Bica (1988). The template which best matches the observed W's listed in Table 3 is the one designated "S2," which represents the typical population of an early type galaxy, with 90% of the light at 5870 Å coming from very old stars (10^{10} yr). The metallicity is about twice solar.

We have used this template to subtract the contribution of the stellar population from each extracted spectrum. Figure 6 illustrates the procedure for the nuclear spectrum. In comparing the template with the data, it was found that several spectra are heavily reddened where the slit crosses the absorption band. By reddening the template spectrum by various amounts, we derived the values of $E(B-V)$ corresponding to different positions, and the results are plotted over the [O III] contours in Figure 5*b*. Comparison of this figure with Figure 5*a* shows that the loci of higher W(Na I) values correspond to the ones with higher $E(B-V)$. The correlation is more clearly

TABLE 3

EQUIVALENT WIDTH OF ABSORPTION LINES

Line	Window (Å)	W (Å)
K (Ca II)	3908–3952	14.8
CN	4150–4214	10.6
G band	4284–4318	9.1
Mg I................	5156–5196	8.2
Hδ	4082–4124	5.3
Hγ	4318–4364	4.3
Hβ	4846–4884	3.4

seen in Figure 5*c*, in which we have plotted W(Na I) versus $E(B-V)$.

3.3. *Emission Lines*

Using the CCD and SIT 5 Å resolution data, we have measured the emission-line intensities in order to investigate the nature of the ionizing source and the characteristics of the gas. In the case of the CCD data, we first subtracted the stellar population template in order to eliminate the effects of underlying absorption. The SIT have has much poorer S/N and no attempt was made to subtract the stellar contribution. Instead, we have corrected the Hα and Hβ emission lines (those most affected by underlying absorption) by the equivalent width of the corresponding absorption line in the stellar template.

Figure 7 show the spatial distribution of the fluxes of the emission lines [O III] $\lambda5007$, Hα, [Ne III] $\lambda3869$, and He II $\lambda4686$ over the galaxy. Although the bulk of the line emission comes from the conical structure to the north of the nucleus and from the elongated feature to the south, there is also faint [O III] and Hα emission from the surrounding region, which was not detected on the images. On the other hand, the higher ionization lines [Ne III] and He II are only observed within the cone (and also in the elongated structure to the south in the case of He II), suggesting a harder ionizing spectrum or increased ionization parameter in these regions. The even higher ionization line [Fe VII] $\lambda6087$ was detected in the nucleus and at $1\rlap{.}''5$ south of the nucleus along p.a. = $10°$.

3.3.1. *Emission-Line Ratios*

We have calculated several interesting emission line ratios in order to study their spatial variation in the galaxy. In the following discussion, we will use the notation [O III] to represent [O III] $\lambda\lambda4959+5007$, [N II] for [N II] $\lambda\lambda6548+6584$, [S II] for [S II] $\lambda\lambda6717+6731$, [O II] for [O II] $\lambda3727$ and [O I] for [O I] $\lambda6300$. When we compared the ratios from the SIT data with those from the CCD data, we found some disagreements for the ratios [O III]/[O II] and Hα/Hβ. The SIT spectra are more subject to systematic calibration errors and to problems with non-Poissonian noise, so we have used the CCD results in cases of discrepancies. Only the ratio [O III]/[O II] was corrected for reddening, which was calculated from the observed Hα/Hβ ratio assuming an intrinsic value of 2.9. We preferred not to correct the other ratios (which are much less sensitive to reddening) because Hβ was too weak to calculate the Balmer decrement in several places where these ratios were measured. We show in Figure 8 the spatial distribution of the emission line ratios [O III]/[O II], [N II]/Hα, [S II]/Hα, and [O I]/Hα.

The [O III]/[O II] ratio is a good indicator of the gaseous excitation or ionization parameter (ratio between the number density of ionizing photons and the number density of particles) and shows that the highest excitation is in the middle and northern part of the cone, as well as in the elongated structure to the south.

The [N II]/Hα ratio presents values that vary from 1 in the middle of the cone (highest excitation region) to 2.5 at the outermost points with detected line emission. [S II]/Hα shows a similar behavior: this ratio is about 0.5 in the highest excitation region and increases to about 1.5 farther out. The [O I]/Hα ratio also shows values that increase away from the center of the cone. In summary, these last three ratios show values that are low in the high-excitation region (as delineated from the [O III]/[O II] ratio) and increase as the excitation gets
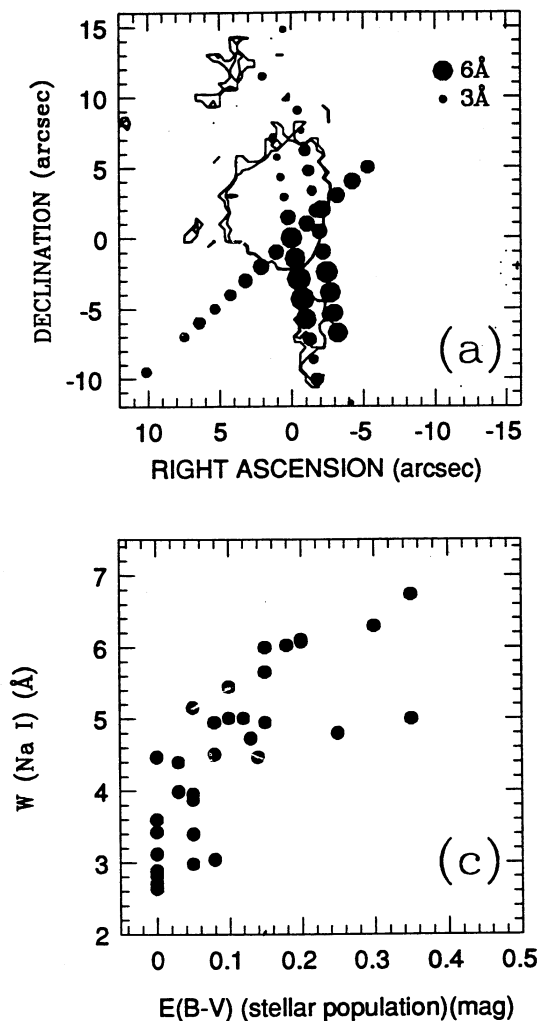
FIG. 5.—(a) Spatial distribution of the equivalent width of the Na I (λ5893) absorption line, W(Na I), superposed on the two outermost isophotes of the continuum-subtracted [O III] emission-line image. (b) Spatial distribution of the reddening values $E(B-V)$ necessary to make the observed continuum slopes match that of the stellar population template (c) Relation between W(Na I) and $E(B-V)$.

lower, indicating that the gradients in the ratios are probably an excitation effect. We will come back to these points later in the discussion (§ 4.3), where we compare the measured ratios with the predictions of photoionization and shock models.

Figure 9a shows the variation of the emission line ratio Hα/Hβ with position in the galaxy, and Figure 9b, the corresponding $E(B-V)_{emission}$, calculated from the observed ratio assuming an intrinsic value of 2.9. Figure 9b can be compared with Figure 5b, which shows the $E(B-V)_{stellar\ population}$ values obtained from the absorption spectrum analysis. Both diagrams indicate a high absorption at the location of the dust lane between the two emission structures, although $E(B-V)_{emission}$ reaches slightly higher values [0.6 as compared with 0.45 for $E(B-V)_{stellar\ population}$].

We show in Figure 9c the variation of the line ratio [S II] λ6717/λ6731 and in Figure 9d the corresponding calculated electron density. It can be seen that the highest densities occur around the apex of the cone, and that the density decreases rapidly going away from the apex.
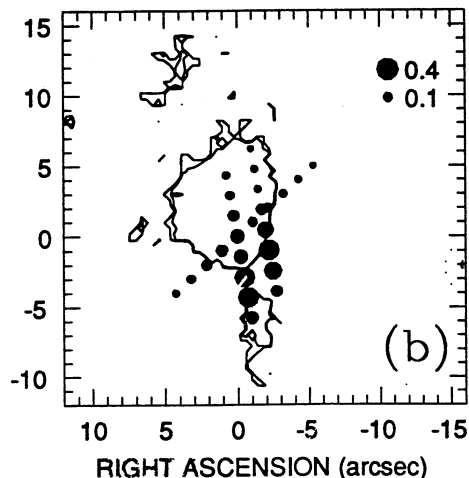
3.3.2. Integrated Fluxes and Mass of Gas

We have summed the [O III] λ5007 and Hα fluxes from the SIT 5 Å resolution data in order to calculate the total luminosity in these emission lines. We have corrected the fluxes for reddening using the Hα/Hβ ratios measured from the CCD data. At places not covered by the CCD spectra, we assumed that no reddening was present. The error introduced by this assumption should be very small, as the CCD spectra cover the regions of stronger emission and reddening. The integrated fluxes are $F([O\ III]) = 1.0 \times 10^{-12}$ ergs cm^{-2} s^{-1} and $F(H\alpha) = 3.7 \times 10^{-13}$ ergs cm^{-2} s^{-1}. The corresponding integrated luminosities are $L([O\ III]) = 2.1 \times 10^{41}$ ergs s^{-1} and $L(H\alpha) = 7.7 \times 10^{40}$ ergs s^{-1}.

The resulting Hβ luminosity [assumed to be $L(H\alpha)/3$] is about 40 times smaller than those of the most luminous Seyfert 2's. We have used the Hβ luminosity to calculate the mass of ionized gas (Osterbrock 1989). Adopting a temperature of 10^4 K and an average density of 200 cm^{-3} (Fig. 9d), the resulting value is $M = 1.2 \times 10^6 M_\odot$.

FIG. 6.—"Nuclear" (peak of λ5461 continuum) spectra of NGC 3281: observed spectrum of the central 1″5 × 1″5 with flux scale and zero point given by the y-axis (top); stellar population template (middle); difference: observed spectrum − template (bottom), after correction for $E(B-V) = 0.15$; for clarity, the template and difference spectra are shifted vertically (the latter by -10×10^{-17} ergs cm^{-2} s^{-1} Å, and the stronger emission lines are truncated in the difference spectrum.
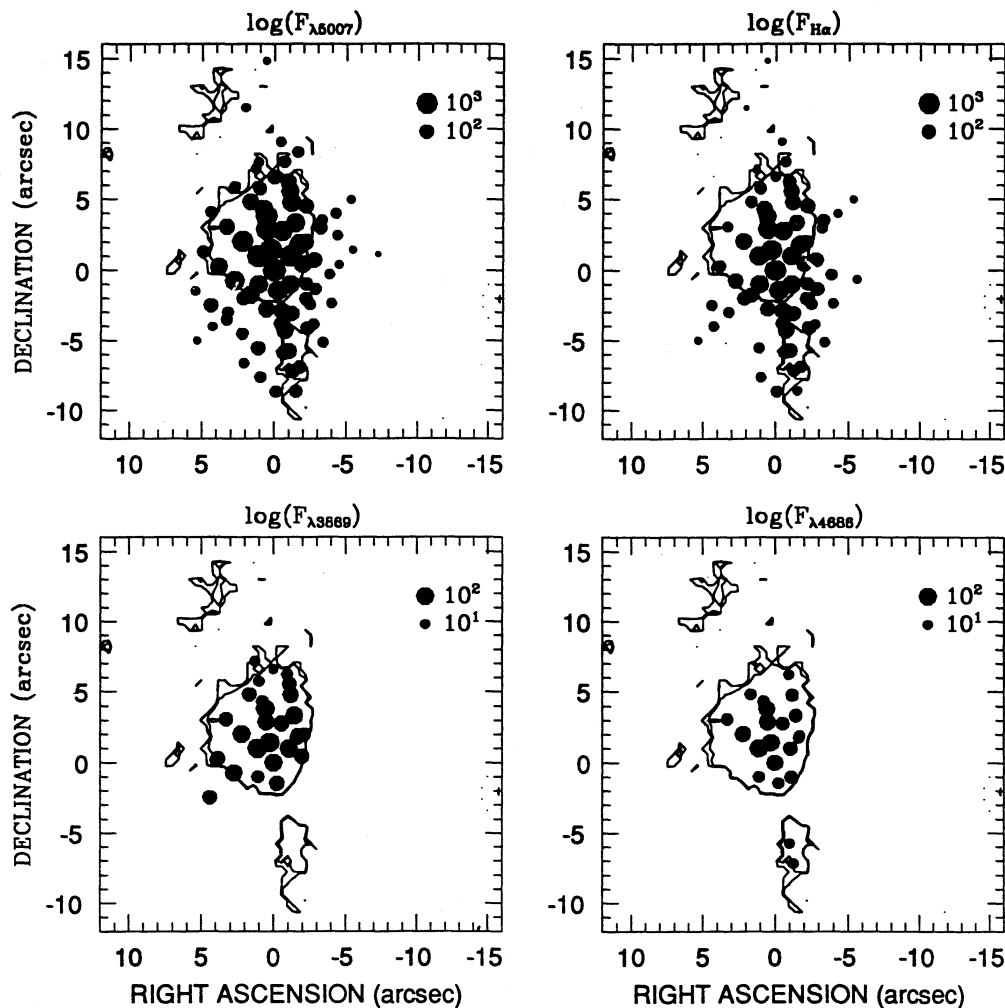
FIG. 7.—Spatial distribution of integrated line emission, as measured from the low-dispersion CCD and SIT spectra, in units of 10^{-17} ergs cm^{-2} s^{-1} arcsec^{-2}. The circles representing the line brightness are superposed on the two outermost contours of the continuum-subtracted [O III] image.

3.4. Line Profiles

We have used the SIT 1.8 Å resolution data to investigate the gaseous kinematics from an analysis of the [O III] $\lambda5007$ and Hβ profiles. As found in the lower spectral resolution long-slit data, there is faint [O III] emission outside the conical region. Figure 10 shows the spatial distribution of the logarithm of the [O III] $\lambda5007$ flux.

3.4.1. [O III] Profiles

The [O III] $\lambda5007$ profiles in the long-slit spectrum along the disk major axis through the apparent nucleus (cf. Fig. 11) are double peaked within the cone. Only the profile from the NW edge of the cone and two others at the SE edge do not have double peaks in this spectrum. These three profiles are also narrower: they have FWHM ≈ 260 km s^{-1} while the ones with double peaks have FWHM ≈ 360 km s^{-1} (after correction for instrumental resolution). In the double-peaked profiles, the two peaks have similar fluxes, and the average velocity difference between them is 130 ± 30 km s^{-1}. The two spectra closest to the nucleus (distance from the peak of continuum light less than 1″) also show "broad" components (FWHM = 900 km s^{-1}). The profiles in the other slit positions have FWHM in the range 170–300 km s^{-1} (after correction for

instrumental resolution); the broader profiles are found at slit positions 1″5 SW and 3″0 NE of the major axis. At this last slit position, two other double-peaked profiles are seen, with the blue peak stronger than the red. Figure 12c shows the positions where a second (redshifted) peak is observed. The other profiles are frequently asymmetric: to the NE of the disk major axis, the asymmetry is in the sense of excess emission to the red of the peak, while in the profiles to the SW of the major axis, the asymmetry is to the blue.

3.4.2. Hβ Profiles

Hβ is much weaker than [O III] $\lambda5007$ and so is not detected as far from the nucleus. The FWHMs have similar values to those found for [O III]. The profiles also show double peaks along the disk major axis, with a velocity difference between the peaks of about 190 km s^{-1}. Two other double-peaked profiles have been found at the slit position 3″ NE of the disk major axis and most profiles are asymmetric, as found for [O III]. Figure 12d shows the positions of the double peaks in Hβ.

3.5. Velocity Field

In order to obtain the gaseous velocity field, we measured the wavelengths of the peaks of Hβ and [O III], calculated the
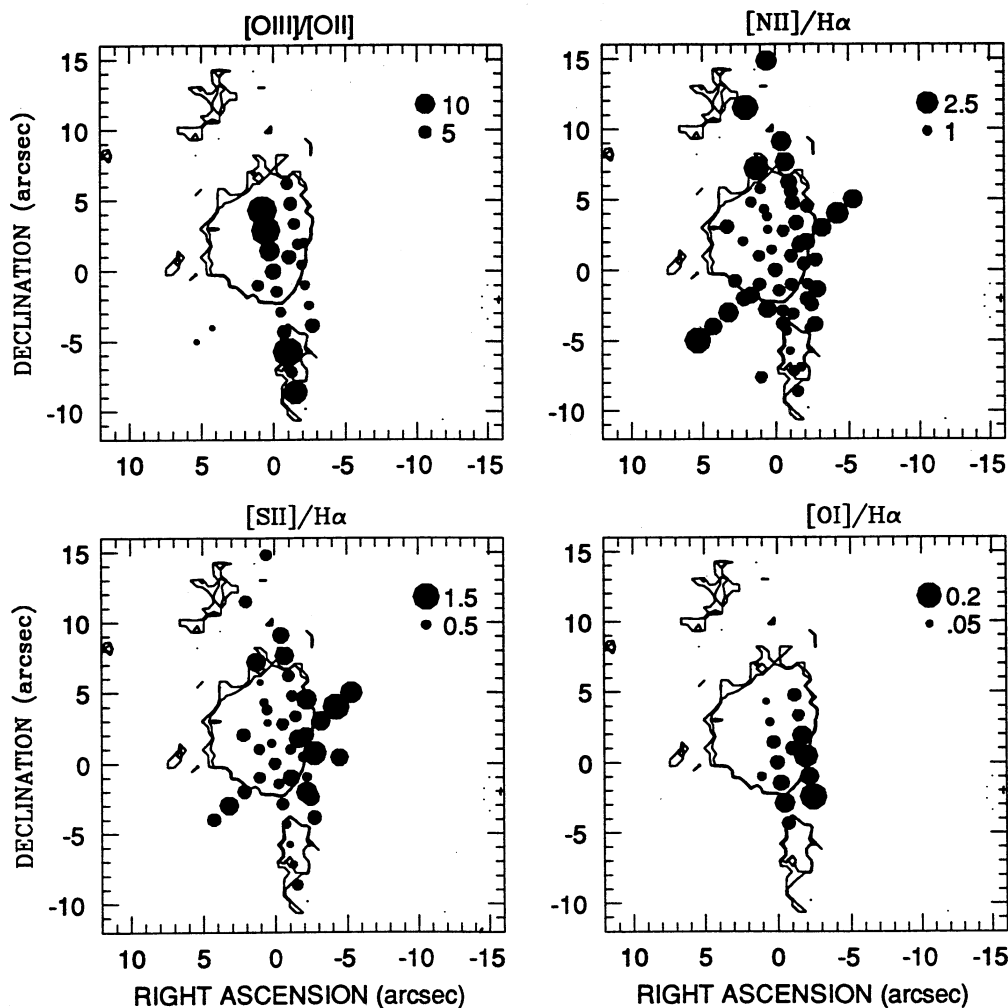
Fig. 8.—Spatial distribution of emission-line ratios, superposed on the two outermost contours of the continuum-subtracted [O III] image. Only the [O III]/[O II] ratio was corrected for reddening (see text).

corresponding radial velocities, and then subtracted the systemic velocity of 3396 km s^{-1}. The resulting observed velocity fields are shown in Figures 12a–12d. We have plotted in Figures 12a and 12b the velocities of the "blue" peaks and the velocities where the lines are single peaked, and in Figures 12c and 12d, the velocities of the "red" peaks. It can be seen that the [O III] and Hβ velocity fields are in good agreement.

Figures 12a and 12b show a clear trend for the velocities to be blueshifted to the SE and redshifted to the NW, as expected if the gas has significant rotational component. In order to check if there is an additional kinematical component (e.g., outflow or inflow), we need to model the rotational component. We have considered two possibilities: (1) the gas lies in the plane of the galaxy, and so has the same rotation velocity as the disk; (2) the gas extends to high latitudes, nearly perpendicular to the disk, and rotates in circular orbits parallel to (and with the same velocities as) those in the disk.

In order to determine the rotational component in these two cases, we must first model the rotation curve of the galaxy. RBFT have measured the rotation curve of NGC 3281 using image-tube spectrograms centered near Hα with the slit aligned along the disk major axis through the nucleus. These authors obtained the rotation curve from the Hα and [N II] emission lines detected out to 30″ SE of the nucleus, and from

the [N II] lines alone on the NW side reaching 35″ from the nucleus. RBFT's measurements have a large scatter within a radius of 10″ from the nucleus (where we have concentrated our study), clearly showing the presence of non-circular motions. RBFT used only the data external to 10″ in order to obtain a mean rotation curve for the galaxy, the systemic velocity being obtained as the center of symmetry of the rotation curve.

We have fitted the following analytical expression to the rotation curve obtained from the data of RBFT along the major axis:

$$V(r) = Ar/(r^2 + C_0^2)^{(p/2)}$$

This expression is given by Bertola et al. (1991, eq. [1]) and assumes that the gas is in circular orbits in a plane.

We have used a chi-square minimization algorithm (Press et al. 1986) to obtain the parameters A, C_0, and p which best reproduce the rotation curve of the galaxy. As $V(r)$ is unconstrained at small r by the RBFT data (so that C_0 will be poorly determined), we have supplemented RBFT's measurements with some of our own close to the nucleus. As the velocity fields of [O III] and Hβ are similar (to within 30 km s^{-1}) and the [O III] profiles have a better S/N ratio and extend farther from
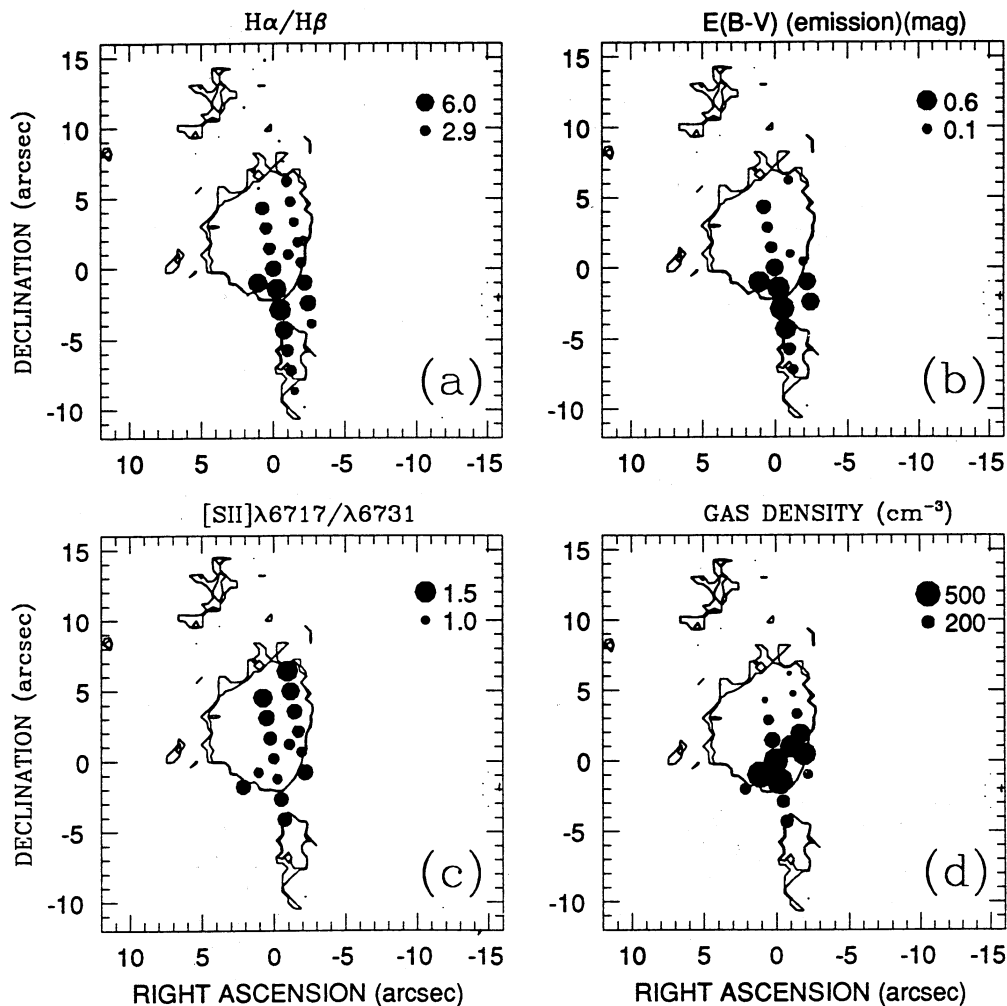
Hα/Hβ

E(B-V) (emission)(mag)

[SII]λ6717/λ6731

GAS DENSITY (cm⁻³)

FIG. 9.—Spatial distribution of the reddening and the density of the gas: (a) emission-line ratio Hα/Hβ; (b) gaseous reddening $E(B-V)_{emiss}$ assuming an intrinsic Hα/Hβ ratio of 2.9; (c) ratio between the two [S II] emission lines; (d) gas density calculated from the ratios in (c).

the nucleus than Hβ does, we decided to use only the [O III] measurements, and tried the following two procedures:

1. First, we assumed that the dynamical center coincides with the peak of green continuum light and used the average of the blue and red peaks along the major axis to represent the circular velocity close to the nucleus. These data, together with RBFT's measurements and the best model fit, are shown in Figure 13a. The rms deviation from the curve is 27 km s⁻¹.

2. If, as the images suggest, the nucleus of the galaxy is to the south of the continuum peak and hidden by the dust lane and if the dynamical center coincides with this nucleus, the "real" major axis would be approximately 1″.5–2″.0 to the SSW of the apparent one. As we have spectra displaced 1″.5 SW of the nucleus, we also used these data to obtain a velocity curve and found a better model fit, with an rms deviation of 15 km s⁻¹. In this calculation we assumed that the center is displaced by $\Delta\alpha = -1″.1$ and $\Delta\delta = -1″.0$ relative to the peak of continuum light. Figure 13b shows the data and fitted curve.

We decided to adopt the second model because of the likelihood that the dynamical center is displaced from the continuum peak and the smaller rms deviation between data and model, although the difference in the quality of the fit between the two models is of the order of the observational errors. The

fit parameters—$A = 193$ km s⁻¹, $C_0 = 4″.9$, and $p = 0.98$— were then used to calculate two-dimensional model rotational velocity fields for the two cases mentioned above: (1) the gas lies in the disk, and (2) the gas extends nearly perpendicular to the disk but the rotational motions are the same as, and parallel to, those in the plane.

The two-dimensional model velocity field of the galaxy was calculated using equation (2) of Bertola et al. (1991), which gives the observed radial velocity of the disk as a function of position in the plane of the sky. Figure 14a shows a representation of this model at the loci corresponding to the observed spectra. The second model was constructed by reproducing the rotation curve along the major axis at all the positions of the long-slit spectra. This model is illustrated in Figure 14b.

Both models were subtracted from the data. Although the residuals are qualitatively similar, the sharp edges of the [O III] images, as well as the abrupt fall of the gas density outside the cone (Fig. 9d), favors a model in which the gas extends to high latitudes above the plane, instead of lying in the disk of the galaxy. The second model, which considers that the high-latitude gas rotates with orbits parallel to those in the galaxy disk, should describe the rotational component of motion of the gas better than the projected disk velocity field. We decided
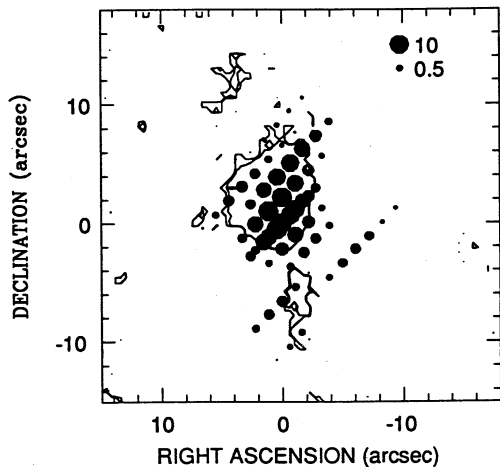
FIG. 10.—Spatial distribution of the logarithm of the flux of the [O III] emission, as measured from the higher dispersion SIT spectra, in units of 10^{-15} ergs cm^{-2} s^{-1} (per spatial resolution element).
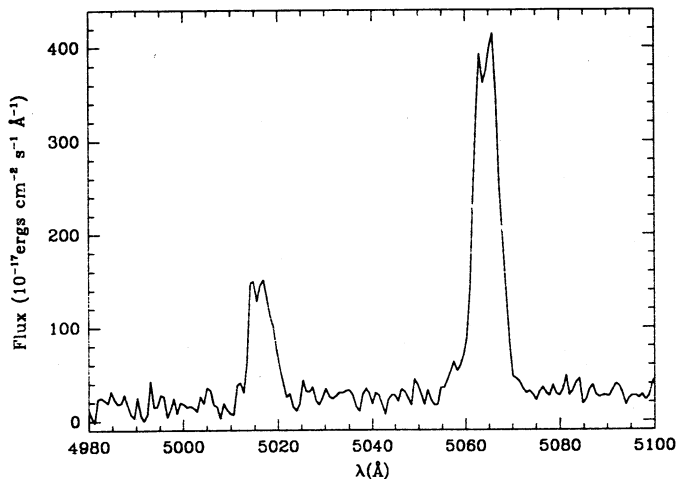

FIG. 11.—Observed typical profiles of [O III] $\lambda\lambda4959$, 5007 emission lines from the long-slit spectrum (with 1.8 Å spectral resolution) passing through the continuum peak.
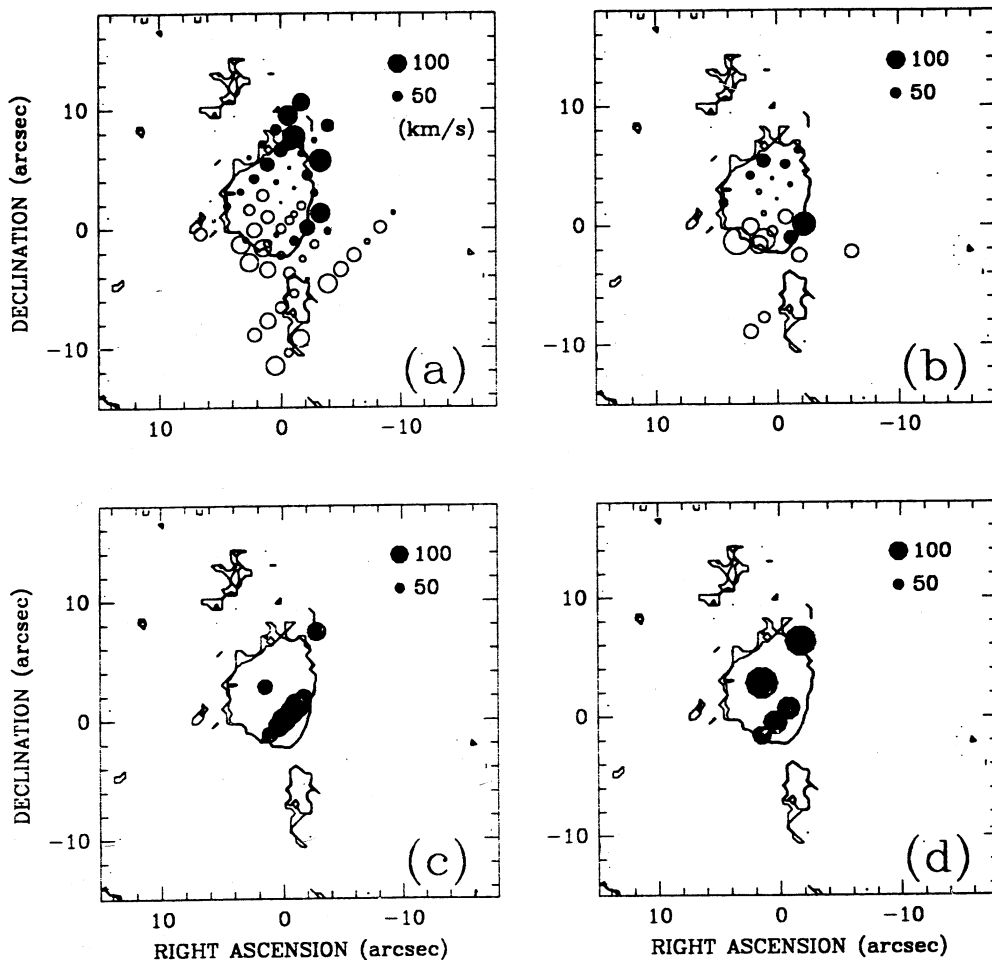

FIG. 12.—Spatial distributions of the peak [O III] $\lambda5007$ and Hβ velocities (relative to the systemic velocity) superposed on the two outermost contours of the continuum-subtracted [O III] image: (a) peak [O III] velocities; (b) peak Hβ velocities; (c) second peak [O III] velocities; (d) second peak Hβ velocities. Open symbols represent blueshifts, and filled symbols, redshifts.
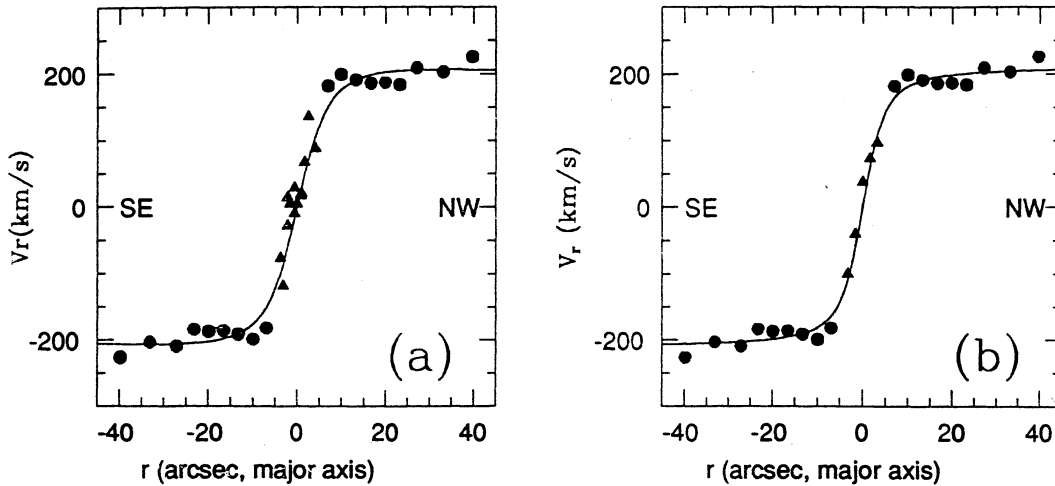
FIG. 13.—Model fits to the major axis velocity data, where circles represent RBFT measurements (produced by averaging the NE and SW sides), triangles represent our measurements, and the continuous lines represent the models. (a) RBFT data, mean velocity of the red and blue peaks in our [O III] profiles along the major axis (assumed to pass through the continuum peak), and best-fit model, with $A = 253$ km s^{-1}, $C_0 = 7\overset{''}{.}7$ and $p = 1.05$ (the origin of the spatial coordinate is at the peak of continuum light). (b) RBFT data, our [O III] data from the observation with the slit displaced $1\overset{''}{.}5$ SW of nucleus, and best-fit model, with $A = 193$ km s^{-1}, $C_0 = 4\overset{''}{.}9$, and $p = 0.98$ (the origin of the spatial coordinate is now at $\Delta\alpha = -1\overset{''}{.}1$ and $\Delta\delta = -1\overset{''}{.}0$ relative to the continuum peak).

to adopt this ("cylndrical") model as a better description of the rotation of the gas and the residuals from it are shown in Figures 15a–15d. It can be seen that most of the residuals in the NE cone are negative. To the SW, there are both positive and negative residuals, with the negative being larger. The SW residuals show a velocity gradient opposite to that of the models.

4. DISCUSSION

4.1. *Geometry and Kinematics of the Emission-Line Gas*

From the morphology of the [O III]–emitting gas we can estimate a projected full cone angle of $\theta = 70°$. This geometry for the high-excitation gas in NGC 3281 is very similar to that observed in NGC 1365 and NGC 7582, although the cone angle seems to be larger in these galaxies (Storchi-Bergmann & Bonatto 1991). The extent of the ionized gas is also similar, reaching a radial distance of 1.5–2.0 kpc. This seems to be a

typical dimension for cones in Seyfert glaxies, as observed, for example, in Mrk 573 (Haniff, Wilson, & Ward 1991; Tsvetanov & Walsh 1991), and NGC 5506 (Wilson et al. 1985). The ionized gas mass is also of the same order (about $10^6\ M_\odot$).

Inspection of Figures 12, 14b, and 15 shows that the cylindrical model seems to account well for the rotation velocities observed in the cone region (first peak), where the rotation pattern is largely eliminated when the model is subtracted. The residuals in the cone region show some SE-NW gradient opposite to that of rotational model (indicating the rotational velocities are slower than we have assumed), but are predominantly negative, suggesting outflow of gas within the cone. The residuals on the SW side also show a pattern opposite to that of the model, indicating that the model does not adequately describe the motion in this region.

A possible picture which accounts for the residual blueshifts and the observed double peaks in the cone region is similar to
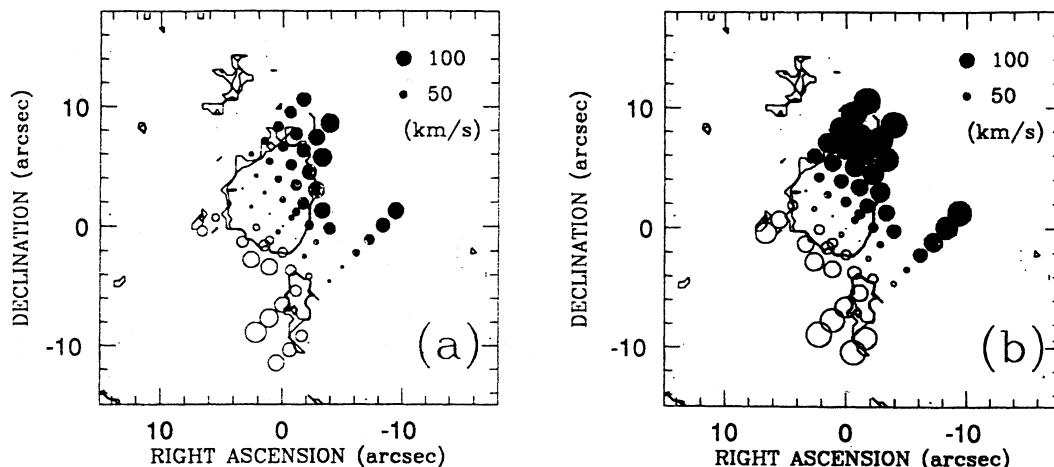

FIG. 14.—Spatial distribution of model peak velocities (see text) superposed on the two outermost contours of the continuum-subtracted [O III] image. Open symbols represent blueshifts and filled symbols redshifts. (a) Model in which the gas is assumed to lie in the galaxy disk; (b) Model in which the gas in the cone is assumed to extend nearly perpendicular to the disk and rotates at the same velocity as gas in the plane with the same distance from the axis of rotation ("cylindrical" model).
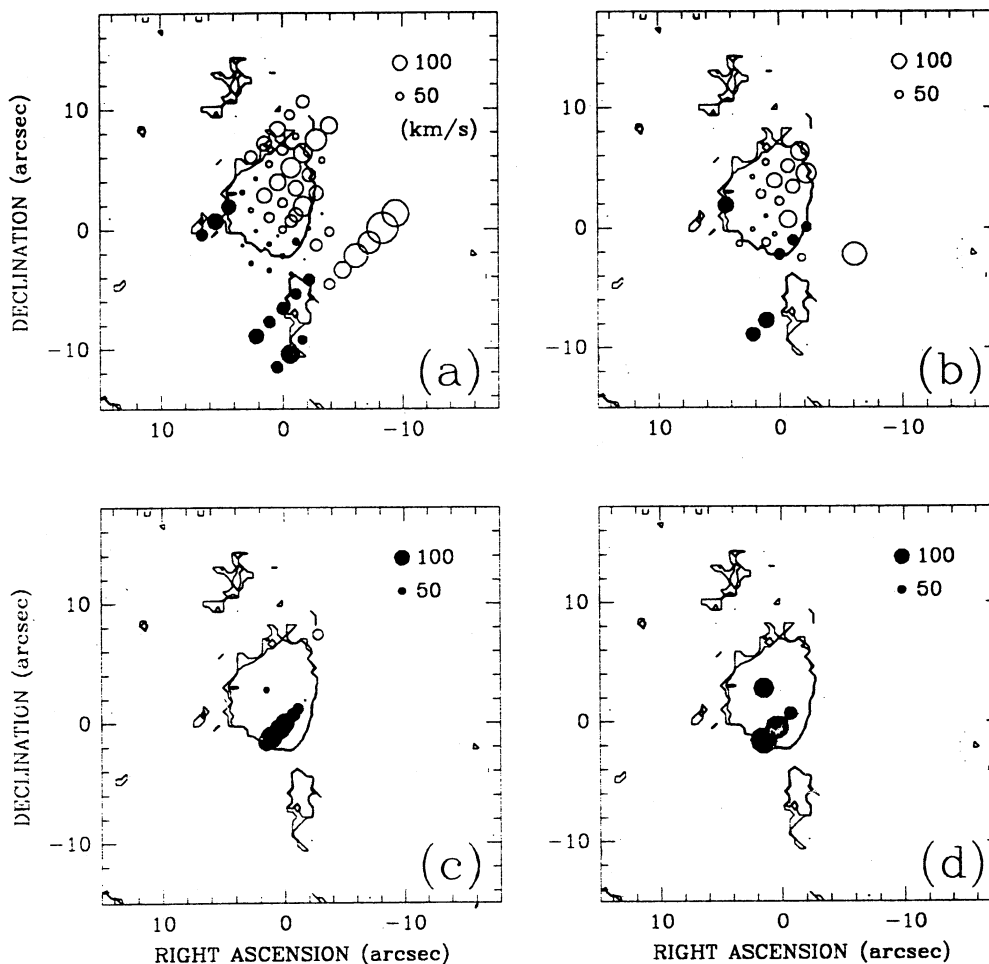
FIG. 15.—Spatial distribution of the residuals: observed peak velocities minus model velocities (see text), superposed on the two outermost contours of the continuum-subtracted [O III] image (a) peak [O III] minus model velocities; (b) peak Hβ minus model velocities; (c) second peak [O III] minus model velocities; (d) second peak Hβ minus model velocities. Open symbols represent blueshifts, and filled symbols, redshifts.

the one proposed by Wilson et al. (1985) for the Seyfert 2 galaxy NGC 5506: outflow of the gas (at velocity V) within a conical envelope or on the surface of a hollow cone. Assuming that the cone's axis is perpendicular to the galactic plane, and thus makes an angle $i_c = 64°$ with the line of sight, the picture would be as sketched in Figure 16a. The near side of the NE cone produces emission which is blueshifted (with velocity V_{blue}) relative to the systemic velocity, while the far side produces redshifted emission (V_{red}). The blueshifted emission observed to the SW of the nucleus could come from either the near side of a counter cone (the observed fluxes being lower because we are seeing the emission dimmed by the intervening disk), or from gas on the near side of the galaxy disk outflowing near the plane and being illuminated by nuclear ionizing radiation. This last possibility is illustrated in Figure 16a, where the SW blueshifted emission is represented by V'_{blue}. Still another possible scenario would be gaseous outflow with a very wide cone (opening angle almost 180°) illuminated by an anisotropic radiation field collimated into a narrower cone, with an opening angle similar to that inferred from the [O III] image (Fig. 2). Nevertheless, as will be seen in the next section, the density drops abruptly outside the observed [O III] emission cone, indicating that the bulk of gaseous outflow is within this cone.

Double-peaked profiles are seen within the cone, 2″–4″ from its apex (Fig. 12). The adjacent profiles at the NW and SE edges of the [O III] cone are single peaked and narrower than those within the cone, in agreement with a conical outflow model for which the velocity splitting is expected to decrease with increasing projected separation from the cone axis. The two other double-peaked profiles (found in the long slit spectrum displaced 3″.0 NE of the continuum peak; see Fig. 12) have their blue component stronger than the red, while all the other profiles in the NE cone show a redward-slanting asymmetry, which is compatible with the existence of a weaker red component coming from the far side of the cone.

We can use the observed velocities V_{blue} and V_{red} from the double-peaked lines along the axis of the cone to calculate the velocity V of the gas along the cone and the inclination i_c of the cone with respect to the line of sight. Along the line of sight to the cone's axis, $V_{blue} = -V \cos (i_c - \theta/2)$ and $V_{red} = -V \cos (i_c + \theta/2)$. Using these two equations, for $\theta = 70°$, we can calculate V and i_c. We have selected the four double-peaked profiles closest to the axis of the cone, where the ratio of the rotational to the radial component of velocity should be negligible. The average values from the [O III] and Hβ profiles are $V_{blue} = -43 \pm 20$ km s^{-1} and $V_{red} = 125 \pm 30$ km s^{-1}, and so $V = 154$ km s^{-1} and $i_c = 109°$. This result indicates that the
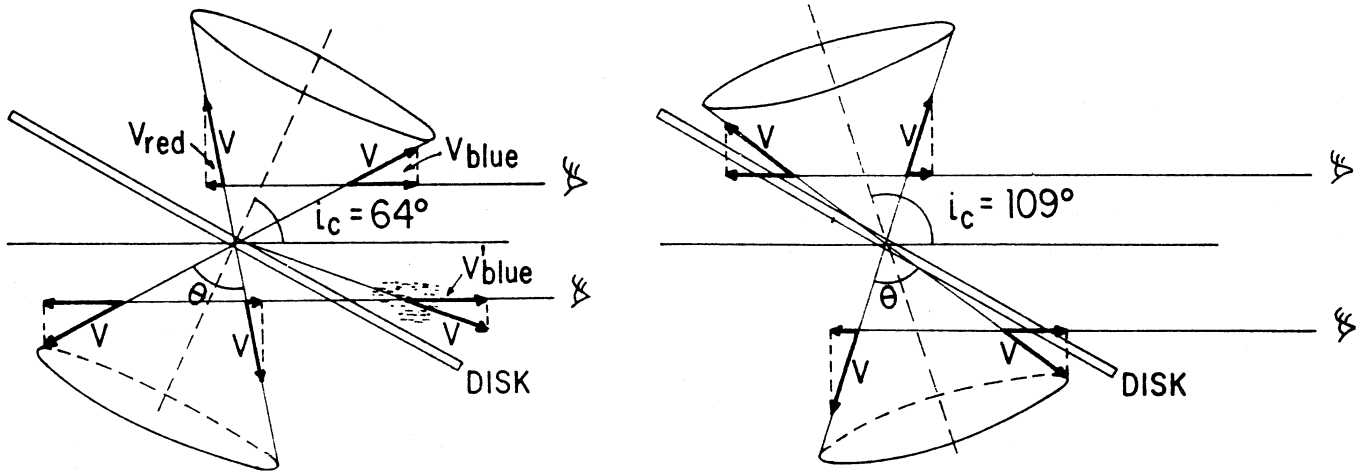
FIG. 16.—Possible schemes for the conical outflow in NGC 3281. The cone may be either filled or hollow (see text). The gaseous outflow velocity V and its projections along the line of sight are shown. (a) The axis of the cone is perpendicular to the plane of the galaxy, and so the angle between its axis and the line of sight is $i_c = 64°$; the double peaks in the cone to the NE of the nucleus result from the blueshifted and redshifted components V_{blue} and V_{red}. The blueshifted emission to the SW of the nucleus could represent excited gas outflowing near the plane with projected velocity along the line of sight represented by V'_{blue}. (b) The cone is tilted relative to the perpendicular plane, and $i_c = 109°$.

cone axis may be tilted relative to the perpendicular to the galactic disk by 45° (Fig. 16b); this is the only way we can get a red velocity component with larger magnitude than the blue, as inferred from these profiles. In this second geometry, it can be seen that the observed large (≥ 100 km s^{-1}) blueshifts to the SW of the nucleus can be accounted for by the partially obscured "countercone." It is interesting to note that the projected cone axis is inclined by $\approx 20°$ to the projected minor axis of the galaxy disk; this also argues that the cone's axis may not be exactly perpendicular to the galaxy disk. The velocity of outflow $V = \Delta V/(2 \sin i_c \sin \theta/2)$ (where $\Delta V = V_{red} - V_{blue}$) is relatively insensitive to i_c, being $V = 163$ km s^{-1} for $i_c = 64°$.

Although outflow in a cone is strongly suggested by our data, the simplest model, in which V, i_c, and θ are independent of distance from the galactic plane, does not fit all the velocity data. For example, there are several values of blueshifts in the cone in the range 60–90 km s^{-1} (after the subtraction of the rotation model) which are larger than the value $|V_{blue}| = 43$ km s^{-1} used above.

In conclusion, it is not possible to obtain a fully self-consistent description of the gaseous kinematics, probably because of uncertain projection effects. However, the following conclusions seem secure: (1) the gas in the NE cone rotates with a similar velocity to that in the plane of the galaxy; (2) in addition to this rotational component, there are radial motions, not only in the NE cone, but also in the gas SW of the nucleus; (3) these radial motions are predominantly blueshifts, indicating outflow of gas within the cone; (4) the presence of double-peaked profiles in the NE cone is consistent with radial outflow; (5) the angle between the cone's axis and the perpendicular to the galactic plane is uncertain, but probably lies in the range 0°–45°; (6) the outflow velocity along the cone is about 150 km s^{-1}; (7) the nature of the gas to the SW of the nucleus is unclear; it could form a counter cone which is largely obscured by dust in the galactic disk or it could be gas outflowing near the disk, on the near side of the galaxy.

4.2. Analysis of the Density Profile

Inspection of the distribution of gas density over the NE cone (Fig. 9d) shows that the highest densities are found near

the cone apex, and that the density decreases toward the top of the cone. The apex of the cone, as determined from the [O III] image, is displaced by $\Delta\alpha = -0''.2$ and $\Delta\delta = -1''.4$ relative to the peak of green continuum light. Figure 17 shows a plot of the density in the cone as a function of the radial distance from the apex. We have plotted as filled circles points along the axis of the cone (p.a. 10° through the green continuum peak). The open circles correspond to other directions from the cone apex. The largest density values presented by these latter points correspond to positions near the cone apex, suggesting that the gas may be entrained into the outflow from a substantial area of the galaxy disk. We have not included in this plot the measurements at the four locations outside the cone (Fig. 9d). The density at these points shows an abrupt decrease from those
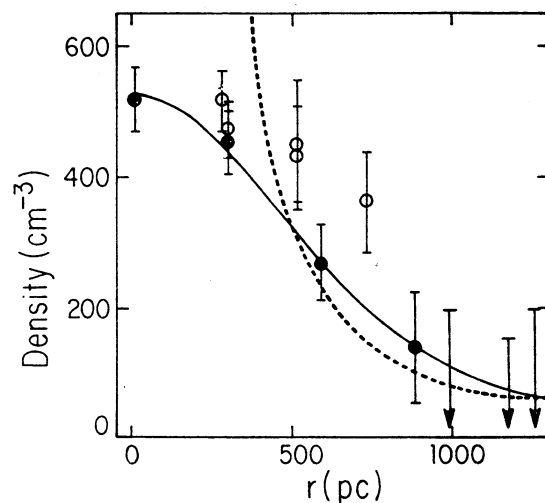

FIG. 17.—Gas density in the cone as a function of distance from its apex. Filled symbols represent points along the axis of the cone, while open symbols represent other locations in the cone. Two curves have been fitted to the points along the axis: an r^{-2} law (dotted line), and the form $n = n_0[1 + (r/a)^2]^{-1}$ (continuous line) with $n_0 = 540$ cm^{-3} and $a = 570$ pc, which is a simple representation of a hydrostatic atmosphere. Note that the r^{-2} form is too steep but the other curve provides an acceptable fit.

just inside the cone, favoring a scenario in which the gaseous outflow is mostly restricted to the cone. Thus, the conical structure may, at least in part, be density limited.

As seen in Figure 17, the density drops off more slowly than $n_e \propto r^{-2}$, which would be the form for a constant velocity, mass conserving wind from a point source. In an AGN, the density profile might be expected to follow such a steep form all the way into the nucleus, while in a superwind driven by a starburst (Chevalier & Clegg 1985; Heckman, Armus, & Miley 1990), the profile flattens at small radii, because the starburst is spatially extended. However, we see no evidence for young stars in NGC 3281 and the narrow apex of the cone strongly favors the Seyfert nucleus as the source of the wind. One possible explanation for the slow drop-off in density is that a hot, low-density wind is driven outward by the nuclear activity (e.g., Krolik & Begelman 1986) and entrains gas from its surroundings (i.e., the wind is not mass-conserving). An observation in favor of this last scheme is the apparent rotational component of motion of the gas in the cone. Gas ejected from very close to the nucleus would have essentially zero rotational velocity in the resolved cone ($\approx$ kpc from the nucleus), because of angular momentum conservation. Gas entrained "in situ," however, would retain a substantial rotational component. A hot isothermal atmosphere, with cool dense condensations radiating the observed emission lines, is another possibility, and the expected fall-off in density is consistent with the data (Fig. 17). However, the emitting gas again would be expected to have low angular momentum, contrary to the observations. The rotational and outward motions therefore favor a mass-entraining wind.

4.3. The Ionization Mechanism and Ionization Parameter

In order to investigate the nature of the ionizing source for the high-excitation gas, we have compared the observed emission-line ratios with photoionization and shock wave models. The photoionization code CLOUDY (Ferland 1990) was used to calculate the emission line ratios for a constant density nebula ionized by a power-law continuum with $F_\nu = \nu^{-1.5}$. We have also considered shock models from Viegas-Aldrovandi & Contini (1989) for a preshock density of 300 cm^{-3} and shock velocities $100 \leq v_0 \leq 600$ km s^{-1}. The model ratios are plotted with the measured ones in Figures 18a–18d. As noted in § 3.3.1, we prefer to show the line ratios uncorrected for reddening because of the weakness of Hβ. The effect of reddening on [O II]/[O III] can be evaluated in Figure 18b, which is the same diagram as Figure 18a but with this ratio corrected for reddening, where this was possible. The points follow the same trend after correction for reddening. We also show in Figure 18a the effect of a reddening $E(B-V) = 0.5$ (arrow) for the typical ratio [O II]/[O III] = 0.3.

From the figures, it can be seen that the shock models reproduce the observed range of [O III]/Hβ, give somewhat higher values for the [N II]/Hα ratio than the observed values, but predict considerably higher values for the [S II]/Hα and [O II]/[O III] ratios than is observed.

The photoionization models reproduce the observed emission line ratios better. As can be seen in Figures 18a–18d, the trends observed in the line ratios are reproduced by the models, reflecting a varying ionization parameter in the range -2.5 (smallest [O II]/[O III] ratios) $\geq \log(U) \geq -3.5$ ($U = Q/4\pi nr^2 c$, where Q is the number of ionizing photons radiated per second by the point ionizing source, n is the density, r is the distance of the gas from the ionizing source, and c is the speed of light.)

Considering that the densities obtained from the [S II] $\lambda6717/\lambda6731$ ratio are $\leq 10^3$ cm^{-3}, we have calculated a sequence of photoionization models with the density and solar abundances. This sequence is identified by the symbol $\odot$ and is shown as a continuous line in Figures 18a–18d. It can be seen that these models predict too low values for the [N II]/Hα and [S II]/Hα ratios. Therefore, as in previous papers (Storchi-Bergmann & Pastoriza 1989, 1990), we first tried increasing the abundance of all the elements in an attempt to reproduce the high [N II]/Hα and [S II]/Hα ratios. The results comprise similar sequences to those for solar abundances and are represented by the dashed lines in Figures 18a–18d. In the context of "pure" photoionization models, the only way to produce the observed higher [N II]/Hα and [S II]/Hα ratios is to selectively enhance the abundances of nitrogen and sulfur to about three times solar. We then obtain the sequences identified by "3N, 3S" and represented by continuous lines, which give a better fit to both the observed [N II]/Hα and [S II]/Hα ratios. The diagram [O III]/Hβ versus [O II]/[O III] (Fig. 18d) is also somewhat better reproduced by these models; the sequence of solar abundance model is displaced relative to the data.

Another possible way of reproducing the high [N II]/Hα and [S II]/Hα ratios, while retaining a high [O III]/Hβ ratio, could be to drive shock waves through a photoionized gas, as suggested by Weaver et al. (1991) for NGC 1386. We have thus compared our emission-line ratios with the models of Viegas-Aldrovandi & Contini (1989) for clouds subjected to both photoionization and shock-wave heating. Although we could obtain high [N II]/Hα, [S II]/Hα, and [O III]/Hβ ratios simultaneously, the presence of shocks also enhances [O II] $\lambda3727$, giving [O II]/[O III] ≈ 1, while the observed ratios are much smaller.

In conclusion, a comparison of the observed emission-line ratios with model values rules out shocks as the primary ionization mechanism. The sequences of line ratios are very well described by photoionization models with varying ionization parameter. If the density of the gas is everywhere $\leq 10^3$ cm^{-3}, as indicated by the [S II] lines, it is necessary to selectively enhance the nitrogen and sulfur abundances to about 3 times solar in order to reproduce the observed [N II]/Hα and [S II]/Hα ratios.

We have used the photoionization models described above to obtain the spatial distribution of the ionization parameter from the observed emission line ratios. Figure 19 shows the results: the ionization parameter increases away from the apex along the axis of the cone. A similar increase of the ionization parameter with increasing distance from the ionizing source has been found in other Seyfert galaxies, like Mrk 573 (Tsvetanov & Walsh 1991), IC 5063 (Colina, Sparks, & Macchetto, 1991) and in some extended emission-line regions around radio galaxies (Robinson et al. 1987). The most straightforward explanation of such a variation in the ionization parameter is that the density drops off faster than r^{-2}. However, our limited density measurements (Fig. 17) do not support this explanation. An alternative possibility is suggested for NGC 3281 by the excellent anticorrelation between the ionization parameter (Fig. 19) and the reddening of the emission lines (Fig. 9c). Perhaps the emission lines found near the apex of the cone (where the reddening is large) originate in gas which "sees" a partially obscured nuclear ionizing source, resulting in a low ionization parameter. Along the axis of the
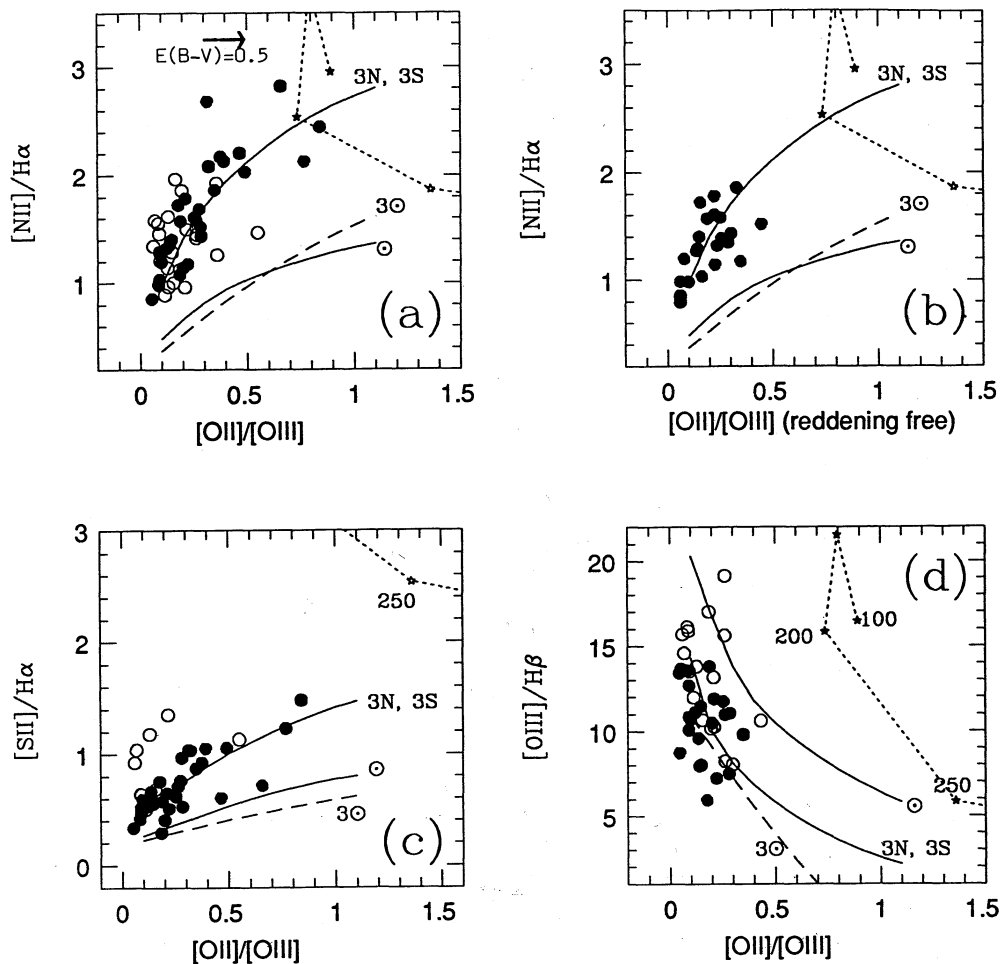
FIG. 18.—The measured emission-line ratios are compared with a number of models. The CCD data are represented by filled symbols and the SIT data by open symbols. The dotted line represent shock models for the velocities indicated in (d), while the other lines represent photoionization models for a gas density $n = 10^3$ cm^{-3} and ionization parameter in the range $-2.5 \leq \log U \leq -3.5$. Models with solar abundance are represented by a continuous line identified by the symbol ⊙; models with nitrogen and sulfur 3 times solar are represented by a continuous line identified by 3N, 3S; the dashed line labeled 3⊙ shows models with the abundance of heavy elements enhanced to 3 times solar. Panel (b) is the same plot as panel (a), but the points have been corrected for reddening using the measured Balmer decrement Hα/Hβ; this correction was applied only to the CCD data. The arrow in panel (a) shows the effect of reddening corresponding to $E(B-V) = 0.5$ for [O II]/[O III] = 0.3.

cone, the path from the nucleus to gas would be clear of dust and the ionization parameter correspondingly higher. This notion would be consistent with the trend for the ionization parameter to be lower away from the axis of the cone than on axis (Fig. 19).

4.4 Obscuration and the True Nuclear Luminosity

We have compared our measurements of the D lines equivalent width W(Na I) (Fig. 5) with the results of Bica & Alloin (1986). Adopting their relation between W(Na I) and W (Mg I) for a stellar population free of absorption by interstellar gas, the expected W(Na I) for NGC 3281 would be 3.3 Å, which is close to the minimum value observed (Fig. 5). Values of W(Na I) in excess of this minimum result from interstellar absorption, as indicated by their correlation (Fig. 5c) with the independently derived values of $E(B-V)$. After subtraction of the contribution of the stellar atmospheres from the measured W(Na I), the highest values found are ≈ 3.5 Å, which are similar to the highest values found in the whole sample of 165 galaxies of Bica & Alloin (1986). The corresponding highest values of $E(B-V)$ for the stellar population are ≈ 0.45, which
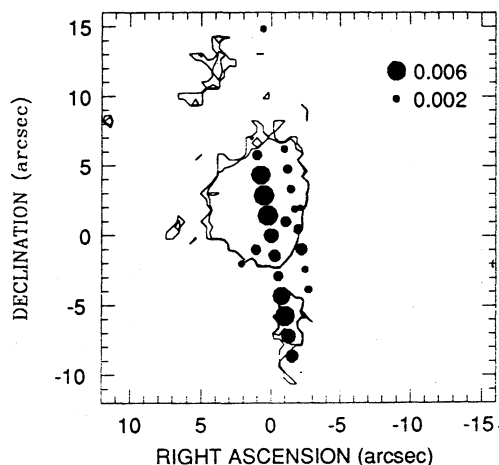

FIG. 19.—Spatial distribution of the ionization parameter superposed on the two outermost contours of the continuum-subtracted [O III] image.

is also similar to the highest values found in Bica & Alloin's sample. Although the highest obscuration is found at the apex of the cone (the presumed location of the true nucleus), its value is similar to those found in normal galaxies with similar inclination to NGC 3281. This result indicates that the reddening observed is simply a consequence of the presence of normal quantities of dust in the disk of the galaxy. Although the Hα/Hβ emission-line ratios give a slightly higher reddening [$E(B-V) \approx 0.65$], those results too are generally consistent with normal amounts of reddening.

As indicated in previous works (e.g., Wilson et al. 1988; Kinney et al. 1991), the narrow-line region in Seyfert 2 galaxies is frequently found to be illuminated by a greater ionizing flux than is inferred by direct observations of the UV continuum, indicating that the active nucleus is either an intrinsically anisotropic radiator of UV photons (e.g., Madau 1988; Acosta-Pulido et al. 1990) or that our direct line of sight to it is blocked by dust (Antonucci & Miller 1985; see Wilson 1992 for a recent review of the evidence for anisotropy). The obscuration is certainly larger than that indicated by the above discussed values of $E(B-V)$; we have found a minimum obscuration of $A_V = 6$ mags to the nuclear nonstellar continuum source based on the following assumptions:

1. The ionizing source has a spectrum $F_\nu = A\nu^{-1.5}$, as used in the photoionization models. This nonstellar ionizing source is not detected in our spectra (cf. Fig. 6) and we have estimated that its contribution to the continuum around 5200 Å is $\leq 20\%$. This was used to calculate an upper limit to the constant A in the above expression for the ionizing flux.

2. From the upper limit to A, we obtain an upper limit to the number of ionizing photons at Earth ($N_{ion} < 6.1 \times 10^{-3}$ photons cm^{-2} s^{-1}) and compare with the total number of Balmer recombination photons at Earth inferred from the observations [$N_{rec} = 8.6N(H\beta) = 0.27$ photons cm^{-2} s^{-1}] with the result $N_{rec}/N_{ion} \geq 44$.

3. If the ionizing source emits isotropically, we expect $N_{rec}/(N_{ion} C) = 1$, where C is the covering fraction of optically thick gas as seen from the nucleus. For a single cone (we effectively detect emission from only the NE cone) with full angle 70° (as suggested by Fig. 2), $C \leq 0.09$ (the upper limit allows for the presence of optically thin gas in the cone). Thus, our observations indicate $N_{rec}/(N_{ion} C) \geq 490$, a large discrepancy with the simple isotropic model. If the UV source is an intrinsically isotropic radiator, then we require $A_V \geq 6$ mag to hide it. Alternatively, the source may be intrinsically anisotropic.

Obscurations of the same order as the lower limit estimated here have been found for the broad-line region of two warm *IRAS* Seyfert galaxies (Hines 1991). The optical spectra of these galaxies are typial of Seyfert 2 activity, but they show broad Paschen-α emission in the infrared spectra, indicating the presence of a hidden Seyfert 1 nucleus. Similar infrared observations of NGC 3281 would better constrain the obscuration to its nucleus. One much more extreme case is the obscuration of $A_V \approx 50$ mag found toward the active nucleus of the radio galaxy Cygnus A (Ward et al. 1991; Djorgovski et al. 1991).

4.5 The Number of Ionizing Photons and the Covering Factor

The ionization parameter, U (Fig. 19), allows us to calculate the number of ionizing photons (as seen by the gas) emitted by the nuclear continuum source per second. When scaled to the

distance of Earth, the flux of these ionizing photons is

$$N_{ph} = Unr^2c/R^2 \text{ photons cm}^{-2} \text{ s}^{-1} ,$$

where R is the distance of the galaxy. This calculation gives $N_{ph} = 6.3 \pm 2.6$ photons cm^{-2} s^{-1}.

The ratio between the number of recombination photons N_{rec} obtained in the previous section and the number of ionizing photons, N_{ph} is equal to the covering factor, C. The value obtained for this ratio is $N_{rec}/N_{ph} = 0.04$, about half the value of the covering factor of a single optically thick cone. This result indicates that the covering factor of the gas within the cone is about 0.5.

4.6. The Origin of the Mid- and Far-Infrared Emission

Assuming that the central source is an isotropic radiator and that it is obscured by a dusty torus, this torus would intercept a fraction 0.82 of the luminosity of the source (the bicone accounting for the other 0.18). We can calculate the infrared emission of the torus through the following steps:

1. Assuming that the ionizing continuum has the spectral shape $L_\nu = A\nu^{-1.5}$, we can calculate A from the number of ionizing photons N_{ph} obtained in the last section; the result is $L_\nu = 2.44 \times 10^{51} \nu^{-1.5}$ ergs s^{-1} Hz^{-1}.

2. The spectral range which efficiently heats the dust is from 100 Å to 1 μm. Integrating the source luminosity in this spectral range and multiplying by the covering factor of the torus (= 0.82) we find $5.3 \pm 2.2 \times 10^{10}$ $L_\odot$, which agrees to within the errors with the infrared luminosity obtained from the *IRAS* fluxes $L_{IR} = 3.4 \times 10^{10}$ $L_\odot$.

This result favors the picture in which an obscuring torus is present and indicates that all the *IRAS* luminosity can be explained by infrared emission from this torus.

5. SUMMARY

We have analyzed narrow-band images and long-slit spectroscopy of the low-luminosity Seyfert 2 galaxy NGC 3281. The main results are as follows:

1. The high-excitation gas exhibits a conically shaped morphology, which is projected against the far side of the galaxy disk and seems to extend to ≈2 kpc of the galactic plane; a possible counterpart cone structure on the other side of the plane is partially seen, being dimmed by obscuration in the galaxy disk.

2. The apex of the cone is displaced about 1″5 (300 pc) from the peak of the green continuum emission.

3. The ratio between the red and green continuum images shows increasing obscuration towards the apex of the cone, reaching $A_V = 1.4$ mag at the apex. This result indicates that the true nucleus is probably hidden, is located near the apex, and does not coincide with the peak of continuum light.

4. Another piece of evidence indicating a hidden nucleus is the absence of dilution of the stellar absorption lines in the nuclear region. An estimate of the obscuration toward the nucleus based on a comparison between the ionizing flux received by the emission-line gas and that emitted toward Earth indicates $A_V \geq 6$ mag.

5. The stellar population is old and typical of early-type galaxies, reaching a metallicity about 2 times solar, and is uniform within a radius of 2.3 kpc from the nucleus. The only absorption line whose equivalent width varies in this region is the Na I D line, which maps well the interstellar obscuration (as inferred from the ratio between the red and green continuum images), and seems to reach a saturation value (3.5 Å) at

the locations of highest obscuration (at and near the cone's apex).

6. The emission-line ratios are consistent with a gas photoionized by a power-law continuum, with nitrogen and sulfur abundances enhanced to 3 times the solar value; the observed gradients in the emission-line ratios are well described by sequences of varying ionization parameter. The ionization parameter increases with increasing distance from the nucleus toward the middle and top of the cone.

7. Double-peaked emission-line profiles, typical of models with outflow in a conical geometry, are seen in and near the ionization cone. The kinematics of the gas shows a rotational component plus outflow within the cone at a velocity of about 150 km s^{-1}.

8. The observed outflow in NGC 3281 has some similarities with starburst driven winds: the values of central density, the density profile, the observed double peaks, and the magnitude of the velocity splitting. Nevertheless, the spectra show no evidence for the presence of young stars and the nebulosity does not show signatures of shocks. The outflow is presumably driven by the obscured Seyfert nucleus.

9. Comparison between the upper limit to the number of ionizing photons inferred from the optical continuum and the observed number of Balmer recombination photons reveals a large discrepancy: $N_{rec}/(N_{ion} C) \geq 490$ (where C is the covering factor). The ionizing source must, therefore, be either blocked from direct view or an intrinsically anisotropic radiator.

10. The covering factor, obtained from a comparison between the number of ionizing photons emitted by the nuclear continuum source (as estimated from the ionization parameter) and the number of Hβ photons emitted by the gas, has a value equal to about half that of the (single) cone. The covering factor of gas within the cone is, therefore, about half.

11. Given the luminosity of the ionizing source and the covering factor of the torus, we have calculated the expected infrared luminosity of the torus $5.3 \pm 2.2 \times 10^{10} L_{\odot}$, which is close to the luminosity inferred from the *IRAS* fluxes of NGC 3281. The nuclear nonstellar continuum source is, therefore, probably an approximately isotropic radiator and the observed mid- and far-infrared emission results from reprocessing of radiation from the source by the dusty torus.

REFERENCES

Acosta-Pulido, J. A., Pérez-Fournon, I., Calvani, M., & Wilson, A. S. 1990, ApJ, 365, 119
Antonucci, R. R. J., & Miller, J. S. 1985, ApJ, 297, 621
Bertola, F., Bettoni, D., Danziger, J., Sadler, E., Sparke, L., & de Zeeuw, T. 1991, ApJ, 373, 369
Bica, E. 1988, A&A, 195, 76
Bica, E., & Alloin, D. 1986, A&A, 166, 83
Boisson, C., & Durret, F. 1986, A&A, 168, 32
Chevalier, R. A., & Clegg, A. W. 1985, Nature, 317, 44
Colina, L., Sparks, W. B., & Macchetto, F. D. 1991, ApJ, 370, 102
Corbin, M., Baldwin, J. A. & Wilson, A. S. 1988, ApJ, 334, 584
de Vaucouleurs, G., de Vaucouleurs, A., & Corwin, H. G., Jr. 1976, The Second Reference Catalogue of Bright Galaxies (Austin: University of Texas Press) (RC2)
Djorgovski, S., Weir, N., Matthews, K., & Graham, J. R. 1991, ApJ, 372, L67
Durret, F., & Bergeron, J. 1988, A&AS, 75, 273
Ferland, G. J. 1990, OSU Internal Report 90-0001
IRAS Point Source Catalog 1985, Joint IRAS Science Working Group (Washington, DC: US Government Printing Office)
Haniff, C. A., Wilson, A. S., & Ward, M. J. 1988, ApJ, 334, 104
———. 1991, ApJ, 368, 168
Heckman, T. M., Armus, L., & Miley, G. K. 1990, ApJS, 74, 833 (HAM)
Heckman, T. M., Blitz, L., Wilson, A. S., Armus, L., & Miley, G. K. 1989, ApJ, 342, 735
Hines, D. C. 1991, ApJ, 374, L9
Kinney, A. L., Antonucci, R. R. J., Ward, M. J. Wilson, A. S., & Whittle, M. 1991, ApJ, 377, 100
Krolik, J. H., & Begelman, M. C. 1986, ApJ, 308, L55
Madau, P. 1988, ApJ, 327, 116
Miley, G. K., Neugebauer, G., & Soifer, B. T. 1985, ApJ, 293, L11
Miller, J. S., & Goodrich, R. W. 1990, ApJ, 355, 456
Morris, S., Ward, M., Whittle, M., Wilson, A. S., & Taylor, K. 1985, MNRAS, 216, 193
Osterbrock, D. E. 1989, Astrophysics of Gaseous Nebulae and Active Galactic Nuclei (Mill Valley, CA: University Science Books).
Phillips, M. M., Baldwin, J. A., Atwood, B., & Carswell, R. F. 1983a, ApJ, 274, 558
Phillips, M. M., Charles, P. A. & Baldwin, J. A. 1983b, ApJ, 266, 485
Phillips, M. M., Turtle, A. J. Edmunds, M. G., & Pagel, B. E. J. 1983c, MNRAS, 203, 759
Pogge, R. W. 1988, ApJ, 328, 519
Press, W. H., Flanery, B. P., Teukolsky, S. A., & Vetterling, W. T. 1986, Numerical Recipes, (Cambridge: Cambridge Univ. Press) 521
Reif, K., Mebold, U., Goss, W. M., van Woerden H., & Siegman, B. 1982, A&AS, 50, 451
Robinson, A., Binette, L., Fosbury, R. A. E., & Tadhunter, C. N. 1987, MNRAS, 227, 97
Rubin, V. C., Burstein, D., Ford, W., Kent, Jr., & Thonnard, N. 1985, ApJ, 289, 81 (RBFT)
Sandage, A. 1978, AJ, 83, 904
Sekiguchi, K. 1987, ApJ, 316, 145
Stochi-Bergmann, T., & Bonatto, C. J. 1991, MNRAS, 250, 138
Storchi Bergmann, T., & Pastoriza, M. G. 1989, ApJ, 347, 195
———. 1990, PASP, 102, 1359
Tadhunter, C., & Tsvetanov, Z., 1989, Nature, 341, 422
Tsvetanov, Z., & Walsh, J. R. 1992, ApJ, 386, 485
Ulvestad, J. S., & Wilson, A. S. 1989, ApJ, 343, 659
Viegas-Aldrovandi, S. M., & Contini, M. 1989, ApJ, 339, 689
Ward, M. J., Blanco, P. R., Wilson, A. S., & Nishida, M. 1991, ApJ, 382, 115
Weaver, K. A., Wilson, A. S. & Baldwin, J. A. 1991, ApJ, 366, 50
Wilson, A. S. 1992, in Physics of Active Galactic Nuclei, ed. S. J. Wagner & W. J. Duschl (Berlin: Springer-Verlag), in press
Wilson, A. S., Baldwin, J. A., & Ulvestad, J. S. 1985, ApJ, 291, 627 (WBU)
Wilson, A. S., Ward, M. J., & Haniff, C. A. 1988, ApJ, 334, 121